Fuel 293 (2021) 120072

Contents lists available at ScienceDirect

Fuel

journal homepage: www.elsevier.com/locate/fuel

Full Length Article

An investigation on early evolution of soot in *n*-dodecane spray combustion using large eddy simulation

Min Zhang [a], Jiun Cai Ong [a], Kar Mun Pang [b], Xue-Song Bai [c], Jens Honore Walther [a,d,*]

[a] Department of Mechanical Engineering, Technical University of Denmark, 2800 Kgs. Lyngby, Denmark
[b] MAN Energy Solutions, Teglholmsgade 41, 2450 Copenhagen, Denmark
[c] Division of Fluid Mechanics, Lund University, P.O. Box 118, S221 00 Lund, Sweden
[d] Computational Science and Engineering Laboratory, ETH Zürich, CH-8092 Zürich, Switzerland

ARTICLE INFO

Keywords:
Spray A
Soot evolution
Soot spike
LES

ABSTRACT

Numerical simulations using large eddy simulation (LES) and Unsteady Reynolds Averaged Navier–Stokes (URANS) are carried out to identify the underlying mechanisms that govern the early soot evolution process in an *n*-dodecane spray flame at 21% O_2 by molar concentration. A two-equation phenomenological soot model is used here to simulate soot formation and oxidation. Both ignition delay time (IDT) and lift-off length (LOL) are found to agree with experimental measurements. The transient evolution of soot mass, in particularly the soot spike phenomenon, is captured in the present LES cases, but not in the URANS cases. Hence, a comparison of numerical results from LES and URANS simulations is conducted to provide a better insight of this phenomenon. LES is able to predict the rapid increasing soot mass during the early stage of soot formation due to having a large favorable region of equivalence ratio ($\phi > 1.5$) and temperature ($T > 1800$ K) for soot formation. This favorable region increases and then decreases to reach a quasi-steady state in the LES case, while it continues to increase in the URANS simulation during the early time. In addition, the soot spike is a consequence of the competition between soot formation and oxidation rates. The time instance when the total soot mass reaches peak value coincides with the time instance when the total mass of soot precursor reaches a plateau. The soot spike is formed due to the continuous increase of oxidizing species in the LES case which leads to a more dominant oxidation process than the formation process.

1. Introduction

Diesel engines with a series of advantages such as strong propulsion, high thermal efficiency and fuel economy have been employed in transportation and other industrial applications. However, in order to comply with the ever more stringent emission regulations and standards, a great amount of effort have been placed to reduce emissions (e.g. soot) from diesel engines.

To better understand the soot formation processes, experimental studies are carried out in a constant volume vessel with controlled ambient density (ρ_{am}) and temperature (T_{am}) conditions which resemble those of direct injection diesel engines [1,2]. A great amount of experimental and numerical efforts are placed in studying Spray A in the Engine Combustion Network (ECN), which uses a nozzle with a diameter of 90 μm to inject *n*-dodecane ($C_{12}H_{26}$) fuel. The baseline ambient conditions for Spray A are standardized to $T_{am} = 900$ K, $\rho_{am} = 22.8$ kg/m^3, and an oxygen (O_2) mole fraction of 15%. A recent progress review [3] has summarized the soot experiments from ECN in investigating the temporal evolution of soot volume fraction (SVF) for Spray A under the baseline ambient conditions. Cenker et al. [4,5] measured the total soot mass in a window with a length of 67.2 mm in the axial direction using the laser extinction coupled with the laser induced incandescence for Spray A under varying O_2 levels (13%, 15%, and 21% mole fraction). For the laser extinction, a modulated HeNe laser beam with the wavelength of 632.8 mm was passed through the soot regions and collected by a collection system which was able to measure the light intensity after passing through the soot regions. The soot optical thickness can be calculated based on the relation between the incident light intensity and the light intensity after passing through the soot regions. Following Mie theory [6], the SVF can be calculated from the obtained soot optical thickness. The spatial distribution of the SVF in a selected cross-section can be qualitatively measured using the laser induced incandescence.

* Corresponding author.
E-mail address: jhw@mek.dtu.dk (J.H. Walther).

https://doi.org/10.1016/j.fuel.2020.120072
Received 14 August 2020; Received in revised form 17 November 2020; Accepted 22 December 2020
Available online 23 February 2021

The measured total soot mass by Cenker et al. [4,5] shows a peak at early time, which then stabilizes and reaches a quasi-steady state (QSS) value. This phenomenon is henceforth known as the soot spike. However, no explanation has been provided in the literature, which is likely due to the limited information about species distribution and obtainable soot chemistry in the measurements.

Numerical models, once being validated, can be used to elucidate different phenomena and expand on the limited details from experimental measurements. To gain a better understanding of the soot formation processes, different soot models (e.g sectional soot model and phenomenological soot model) [7–9] have been proposed to study soot formation processes in Spray A. With the implementation of the well-stirred reactor (WSR) model where turbulence chemistry interaction (TCI) is not considered, Wang et al. [9] and Razak et al. [7] were able to capture the overall steady-state SVF with varying O_2 levels in their Unsteady Reynolds Navier–Stokes (URANS) simulations. However, the soot spike was not captured. It is known that considering TCI has a significant effect on the combustion characteristics, such as ignition delay time (IDT), lift-off length (LOL), and the thickness of the reacting zone [10–13]. Many TCI models have been employed in numerical studies of combustion processes for Spray A with $T_{am} = 900$ K and varying O_2 levels (13%, 15%, and 21% mole fraction). Fernandez et al. [14] who implemented the transported probability density function (TPDF) model with the Euclidean minimum spanning tree (EMST) as the micro-mixing model, were able to capture the soot spike using their URANS setup. However, Chishty et al. [15] who coupled the TPDF model with the interaction by exchange with mean (IEM), were not able to capture the soot spike in their URANS simulation. In addition, Lucchini et al. [16] compared the soot evolution by coupling the tabulated kinetics with three different combustion models: WSR, presumed PDF, and representative interactive flamelets (RIF). Their study showed that RIF is the only model that can capture the soot spike. It is clear that using different TCI models and TPDF micro-mixing models of molecular transport leads to different mixture distribution prediction, which results in different prediction in soot behavior. Although some of the aforementioned works reproduced the experimental trend of early soot evolution observed in ECN, no detailed explanation on the soot transient behavior, in particularly soot spike, is provided.

It is noteworthy that all the aforementioned works were carried out in the URANS framework. Aubagnac-Karkar et al. [8] speculated that the large eddy simulation (LES) approach may be able to capture the soot spike phenomenon due to a better prediction of air/fuel mixing. There are various studies on soot formation of Spray A using LES [13,17,18]. However, these works mainly focused on the soot formation processes at the QSS instead of the early stage of soot formation. Setting against this background, the objective of the present study is to investigate the early soot evolution where more emphasis is placed onto identifying the mechanisms behind the formation of the soot spike. This aim is achieved by performing LES of Spray A at different O_2 levels of 15% and 21%. Implicit LES and URANS results are also provided as a comparison with the LES results.

The paper is organized as follows. The case descriptions are provided in Section 2. The numerical methods and computational setup are presented in Section 3. Analysis on the combustion characteristics and transient evolution of soot with a focus on soot spike are shown in Section 4. The conclusion of this work is highlighted in the last section.

2. Case descriptions

The experimental reference cases for the present numerical study correspond to Spray A from ECN. Detailed description of the experimental vessel and measurement methods is provided in [1,19,20]. The injection and operating conditions of Spray A are listed as follows. The fuel injector nozzle diameter, discharge coefficient and half cone angle are 90 μm, 0.89, and 10°, respectively. The injection pressure, injection mass flow rate and injection duration are 150 MPa, 2.295 g/s, and 6.1 ms, respectively. The fuel is *n*-dodecane with a fuel temperature of 373 K. The ambient temperature and density are 900 K and 22.8 kg/m^3, respectively. The ambient O_2 level for the non-reacting case is set to 0%. The reacting spray cases with different ambient O_2 mole fraction (15% and 21%) are representative of the diesel combustion with and without exhaust gas recirculation (EGR).

3. Numerical methods

The simulation work is performed using OpenFOAM-v1712. The computational time step is set to 0.05 μs. Second-order schemes are used for the spatial and temporal discretization. No-slip boundaries are employed to all walls. The computational domain corresponds to the experimental constant volume vessel, which is a cube with a length of 108 mm for each side. In this study, three different meshes (mesh A, B, and C) are used to conduct the mesh convergence study. The details of these three meshes are illustrated in Fig. 1. Mesh A (2.9 million cells) and mesh C (19.1 million cells) have a uniform mesh size of 0.25 mm and 0.125 mm, respectively, in a refined mesh region which covers the whole axial region with a radius of 15 mm. Mesh B (6.0 million cells) has a base mesh of 0.25 mm that covers the spray flame region (15 mm radially and 108 mm axially from the nozzle location) and a finer mesh of 0.125 mm near the nozzle region (6 mm radially and 15 mm axially from the nozzle location). For all three meshes, coarser mesh resolution is used outside the spray flame region.

3.1. LES submodels

In this study, the traditional Lagrangian-parcel Eulerian-fluid approach is used to model the spray, flow, and combustion processes. The injected liquid phase of $C_{12}H_{26}$ fuel is modeled as discrete parcels, where each parcel represents a group of spherical droplets whose position, size, and physical properties are similar. The injection velocity can be calculated based on the mass flow rate and discharge coefficient (cf. Section 2). The primary breakup is considered by injecting computational parcels with the Rosin–Rammler distribution [21]. In the Rosin–Rammler distribution, the maximum droplet size is equal to the diameter of injector nozzle. The minimum droplet size is set to 10% of the maximum droplet size. The mean value of droplet size is set to 70% of the maximum droplet size. Similar settings for the droplet sizes are used in [22,23]. The secondary breakup of the droplets is modeled using the Reitz-Diwakar model [24], where the stripping breakup constant (C_s) is set to 10. The combination of the Rosin–Rammler model and the Reitz-Diwakar model has been widely used to model breakup process of spray [25,26]. Collision between particles is not taken into account due

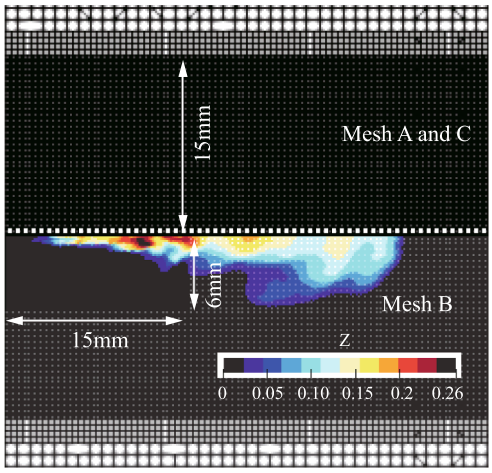

Fig. 1. Cut planes of different meshes (top: mesh A and C, bottom: mesh B) and mixture fraction, Z.

to their minor effect on penetration [27]. The gas phase is described using the spatially filtered transport equations for LES [28,29]. The sub-grid scale is modeled using the dynamic k-equation model [29]. The effect of the resolved flow field on the droplets is modeled by the drag force model [30]. The sub-grid turbulence effect on the droplets is accounted for via a sub-grid droplet dispersion model [31]. In addition, the Ranz-Marshall correlation is employed to calculate the heat transfer between the liquid and gas phases. This model has been used in [15,32].

3.2. Chemical mechanism and combustion model

In this study, the skeletal mechanism developed by Yao et al. [33] is used to simulate $C_{12}H_{26}$ fuel oxidation. This skeletal mechanism consists of 54 species and 269 reactions. The WSR combustion model is employed in the current LES. With this model, the mixture in each cell is assumed to be homogeneous [34,35]. The chemistry coordinate mapping (CCM) approach is used with the WSR model to accelerate the temporal integration of chemical reaction rates. The CCM resolutions are fixed at 5 K, 0.01, 0.025, and 0.001 for temperature, mass fraction of element, scalar dissipation rate, and mass fraction of fuel, respectively. The details of CCM are available in [36–38]. Implementation of WSR-CCM in LES can be found in [18,39].

3.3. Soot model

In order to simulate the soot formation and oxidation processes, a multi-step phenomenological soot model is employed in the present study [32], where the soot model is modified from the one proposed by Leung et al. [40]. The soot model considers soot inception, coagulation, soot surface growth, soot oxidation by O_2 as well as soot oxidation by hydroxyl radical (OH). In this model, acetylene (C_2H_2) is selected as the soot precursor for inception and gas phase molecular adsorption for surface growth. Although polycyclic aromatic hydrocarbon is a better soot precursor, C_2H_2 has been widely used in many studies [13–15,35]. Pang et al. [35] investigated the chemical kinetics on soot formation. They found that C_2H_2 is applicable as the soot precursor when the ambient O_2 level is high. Two transport equations are solved for the soot mass fraction (Y_{soot}) and soot particle number density (ϕ_N). These two equations are expressed as follows:

$$\frac{\partial}{\partial t}(\rho Y_{soot}) + \frac{\partial}{\partial x_j}(\rho u_j Y_{soot}) = \frac{\partial}{\partial x_j}\left(\frac{\mu_t}{Sc_t}\frac{\partial Y_{soot}}{\partial x_j}\right) + \frac{dM_{soot}}{dt} \tag{1}$$

where ρ, u_j, μ_t, and Sc_t denote the fluid density, flow speed, effective turbulent viscosity, and turbulent Schmidt number, respectively, and

$$\frac{\partial}{\partial t}(\rho \phi_N) + \frac{\partial}{\partial x_j}(\rho u_j \phi_N) = \frac{\partial}{\partial x_j}\left(\frac{\mu_t}{Sc_t}\frac{\partial \phi_N}{\partial x_j}\right) + \frac{1}{N_A}\frac{dN_{soot}}{dt} \tag{2}$$

where N_A is the Avogadro number with a value of $6.022045 \times 10^{26}\text{kmol}^{-1}$.

The source term of Eq. (1), $\frac{dM_{soot}}{dt}$, which denotes the net production of soot mass, is expressed as follows:

$$\frac{dM_{soot}}{dt} = MW_c\left(100\omega_{inc}[C_2H_2] + 2\omega_{sg}[C_2H_2] - \omega_{OH}[OH] - \omega_{O_2}[O_2]\right) \tag{3}$$

where MW_c is the molecular weight of carbon atom. The first to fourth terms on the right-hand side of Eq. (3) denote the rate of inception (ω_{inc}), rate of surface growth rate (ω_{sg}), rate of oxidation by OH (ω_{OH}), and rate of oxidation by O_2 (ω_{O_2}). These reaction rates are calculated using the global reaction step using the Arrhenius expression,

$$\omega_i = C_i T^{b,i} \exp\left(\frac{-T_{a,i}}{T}\right) S_{soot}^{n,i} \tag{4}$$

where C_i, T, $T_{a,i}$, and S_{soot} denote the model constant, gas temperature, activation temperature, and soot specific surface area, respectively. The corresponding descriptions and model constants are summarized in Table 1, where p is the gas pressure and p_{ref} is the atmospheric pressure. The model constants are kept the same as those reported in [32]. They were calibrated to predict soot formation in n-heptane fuel spray combustion using URANS.

The source term of Eq. (2), $\frac{dN_{soot}}{dt}$, which denotes the instantaneous production rate of soot particles, is given as follows:

$$\frac{dN_{soot}}{dt} = N_A\omega_{inc} - \omega_{coag} \tag{5}$$

The coagulation rate (ω_{coag}) is expressed as below:

$$\omega_{coag} = C_{coag}\left(\frac{24k_BT}{\rho_{soot}}\right)^{1/2}\left(\frac{6M_{soot}}{\rho_{soot}\pi}\right)^{1/6} N_{soot}^{11/6} \tag{6}$$

where the model constant, soot density, and Boltzmann's consant are $C_{coag} = 3$, $\rho_{soot} = 2000$ kg/m^3, and $k_B = 1.38054 \times 10^{-23}$ J/K, respectively.

Meanwhile, the SVF is calculated from the soot mass fraction and is expressed as follows,

$$\text{SVF} = \frac{\rho Y_{soot}}{\rho_{soot}} \tag{7}$$

4. Results and discussion

4.1. Non-reacting spray characteristics

The validation of the computational setup is first carried out by comparing the liquid penetration length (LPL) and vapor penetration length (VPL) of the inert spray with the experimental data [5]. In the present study, LPL is defined as the maximum axial distance between the spray injector nozzle and the position where 95% of the total liquid mass is observed. VPL is determined using the farthest downstream location of 0.1% fuel mass fraction [5]. A comparison of the measured and simulated LPL and VPL is shown in Fig. 2. The figure also shows the LPL and VPL from three different mesh configurations as mentioned in Section 3. As observed in Fig. 2, the LPL and VPL are overpredicted when mesh A is used, whereas the computed LPL and VPL using meshes B and C show good agreements with the experimental data, indicating that the main liquid spray region has to be sufficiently refined.

4.2. Reacting spray characteristics

The model validation is next carried out using the experimental IDT and LOL of reacting sprays at O_2 levels of 15% and 21%. The computed IDT is defined as the time from start of injection to the time when the maximum rate of maximum temperature rise in the domain occurs [13]. This definition is in accordance to the ECN recommendation [5]. LOL is defined as the shortest distance between the injector and the downstream location where the mass fraction of OH reaches 2% of its maximum value [3]. A mesh sensitivity study is first performed for the 15% O_2 case. As shown in Table 2, there are only small differences in the predicted IDTs for different mesh configurations. The predicted LOLs, which are time-averaged from 1 to 3 ms, show grid convergence for mesh B where local refinement is used. In addition, the ratio of the resolved turbulence kinetic energy to the total turbulence kinetic energy

Table 1
Soot model constant values used in [32].

i	Description	C_i	b	$T_{a,i}$	n
inc.	Inception	10000	0	21000	0
sg	Surface growth	$14(p/p_{ref})^{1.4}$	0	12100	0.5
OH	Oxidation by OH	0.36	0.5	0	1.0
O_2	Oxidation by O_2	10000	0.5	19778	1.0

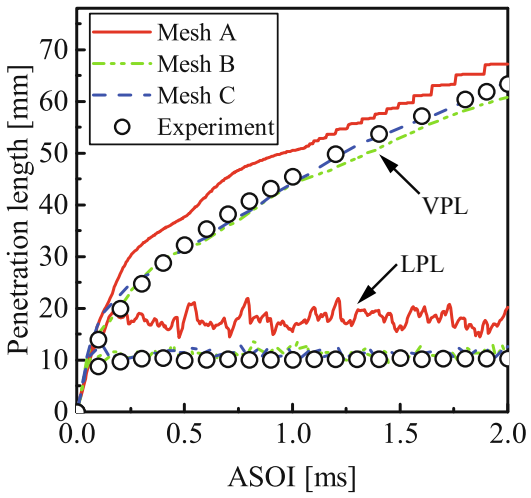

Fig. 2. Liquid and vapour penetration lengths after start of injection (ASOI) for different mesh configurations using LES.

Table 2
Mesh convergence in LES of reacting spray under 15% O_2 ambient gas condition.

Case	IDT (ms)	LOL (mm)
Mesh A	0.318	24.2
Mesh B	0.330	17.2
Mesh C	0.320	16.4
Experiment [5]	0.400	16.0

in the spray region for mesh B is 84%, indicating that the flow is sufficiently resolved by the LES model [41]. To achieve a balance between accuracy and computational efficiency, mesh B is used in all subsequent simulations. For the 21% O_2 case, the predicted IDT and LOL in mesh B are 0.237 ms and 13.2 mm, respectively, which are comparable to the measured IDT of 0.280 ms and measured LOL of 9.9 mm [5]. The relative errors for the predicted IDT and LOL are 15.3% and 33.3%, respectively in the 21% O_2 case when mesh B is used. These values reduce to 17.5% and 7.5%, respectively in the 15% O_2 case. It is important to note that the underpredictions of the IDTs were also reported in [14,42] where the same reduced mechanism was used. Hence, the underprediction of IDT is likely due to the reduced chemical kinetic mechanism used. The overprediction of LOL for the case of 21% O_2 is mainly due to experimental uncertainties. The simulated LOL in this case is close to the measured LOL in [43] where the experimental LOL under the same conditions was reported to be 13.3 mm. In addition, similar overprediction of LOL can be found in [15,42] where the simulation results were compared against the measured LOL of 9.9 mm.

4.3. Temporal evolution of soot

The model performance in predicting the distribution of SVF is assessed. Fig. 3 shows a comparison of predicted and measured temporal evolution of SVF at three different time instances (0.9 ms, 1.2 ms, and 1.5 ms) for the 15% O_2 case. As depicted in Fig. 3, the distribution of the predicted SVF shows good agreements with the experimental results.

The evolution of simulated and measured soot mass for the 15% and 21% O_2 cases is shown in Fig. 4. In the experiment, the total soot mass is only measured within the region from the nozzle to 67.2 mm downstream along the axial direction. Hence, only the simulated soot within this region is considered in the soot mass calculation. As shown in Fig. 4, the LES result from the original soot model underpredicts the soot mass by a factor of 10. This is because the soot model constants used in the original soot model are calibrated for the URANS cases, as shown in [32,44]. Hence, the soot model constans need to be recalibrated for the LES case. The C_{sg} constant in the surface growth model (cf. Table 1) is tuned from 14 to 45 in order for the LES model to predict comparable soot mass to the experimental data. From Fig. 4, both experimental and LES results show a similar trend in their temporal evolution, in which the soot mass increases rapidly to reach a peak and then decreases to reach QSS. This phenomenon is referred to the soot spike in the current study. It should be noted that the experimental results are ensemble-averaged from at least 5 individual events, while the simulations are from a single realization. It is important to note that both the original and tuned soot models are able to capture the formation of soot spike, despite the underprediction of the absolute soot mass value in the former case. This implies that the early soot evolution trend is less sensitive to the change in soot model constants. In the present study, the research goal is focused on the trend of early soot evolution instead of the absolute soot mass value. Hence, only the results from the original soot model in both the LES and URANS cases are analyzed in the subsequent sections.

4.4. Soot spike

As discussed in the previous section, Fig. 4 shows that the current LES model in the literature is able to capture the soot spike, despite using the WSR model. Numerous simulations have shown to be unsuccessful in capturing this soot spike for URANS simulation, unless certain TCI models (e.g. RIF or TPDF with EMST) were applied [15,8]. To

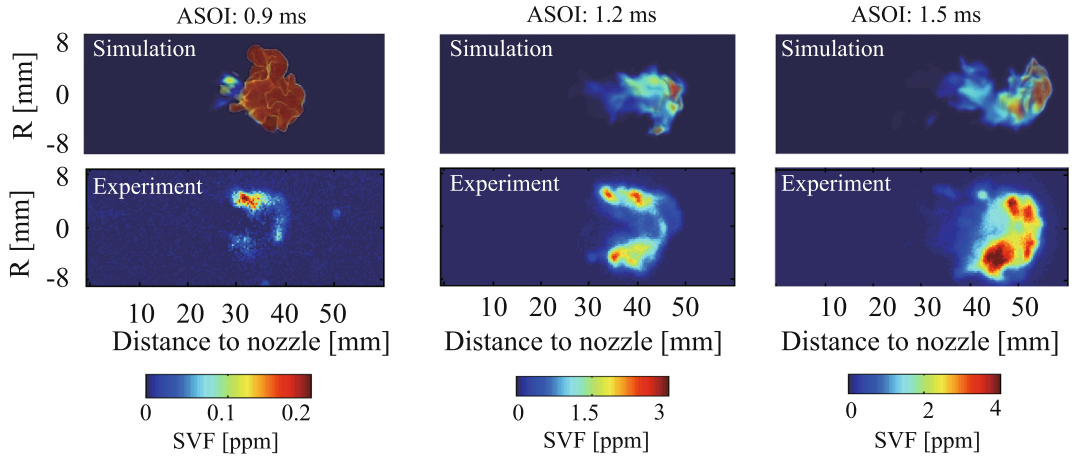

Fig. 3. Comparison of the temporal evolution of predicted (top row) and measured (bottom row) soot volume fraction (SVF) under 15% O_2. The LES simulation results are iso-volume of SVF, while the experimental results are ensemble-averaged SVF from four individual injection events.

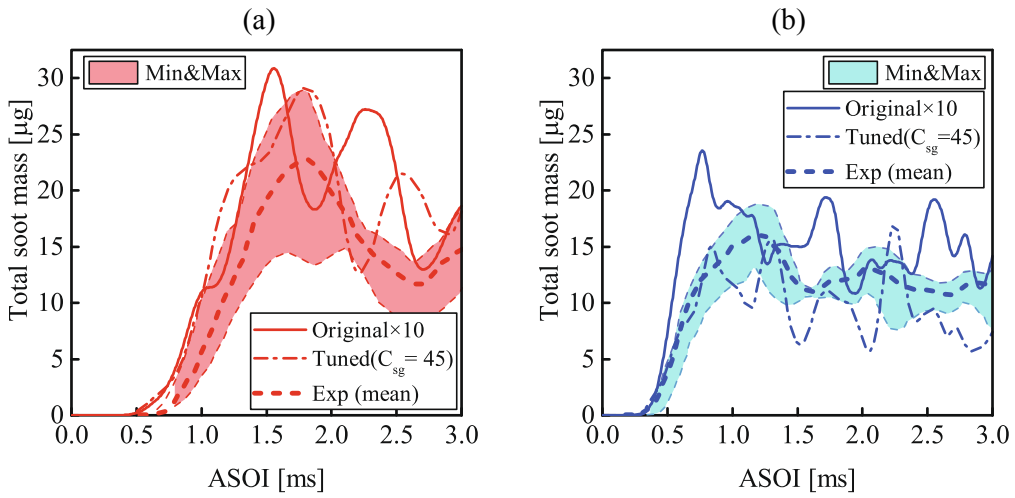

Fig. 4. Comparison of the temporal evolution of soot mass between experimental and simulated results under different O_2 levels: (a) 15% O_2, (b) 21% O_2. Dashed line is used to represent experimental results. Solid line denotes the simulation results with the original soot model. Dashed-dot line denotes the simulation results with the tuned soot model.

investigate the mechanism behind the formation of the soot spike, LES and URANS simulations are performed at 21% O_2. It is also worth further investigating whether the successful prediction of the soot spike in the LES case is due to the sub-grid model. Therefore, an implicit LES case is also performed, in which no LES sub-grid model is used. Validation results of the non-reacting and reacting spray characteristics for the URANS and implicit LES cases can be found in Appendix A. The associated predictions of LPL, VPL, IDT, and LOL are in good agreement with the experimental data. It is also worth highlighting that URANS and implicit LES cases are using the same WSR model as in the LES case. Fig. 5(a) shows the evolution of LOL, which is one of the important combustion characteristics that influence soot formation. One can see that the LOLs for the LES and implicit LES cases are shorter than that for the URANS case. As shown in Fig. 5(b), the soot spike is observed in both the LES and implicit LES cases. The successful prediction of the soot spike in the implicit LES case may be attributed by the fact that more than 80% turbulent kinetic energy is resolved downstream from the injector, where the soot is mainly formed. On ther other hand, the total soot mass for the URANS case increases slowly to reach a QSS while no soot spike is observed. This prediction is similar to those reported in [7,8,15,34]. This implies that the URANS turbulence closure approach is the main reason for the failed prediction of the soot spike formation. Due to the similar prediction of the soot spike in the LES and implicit LES cases, the subsequent analysis is only carried out for the LES and URANS cases to shed light on the difference in the early soot mass prediction. The analysis is solely focused on the 21% O_2 case where the EGR effect is not considered.

It is speculated in [8,15] that a steep gradient of mixture fraction (Z) near the jet head contributes to the formation of the soot spike. Thus, a comparison of the gradient of Z between the LES and URANS cases is illustrated in Fig. 6 where a steep gradient of Z can be observed in both the LES and URANS simulation results. Meanwhile, the gradients of Z in both the LES and URANS simulations fall in the same order of magnitude. Hence, a steep gradient of Z near the jet head may not be the main explanation to the soot spike. As shown in Fig. 5(a), the LOL in the LES case is shorter than that in the URANS case. This shorter LOL may result in a larger favorable region for soot formation in the LES case. However, it should be noted that the shorter LOL is not the only reason for the larger favorable region for soot formation in the LES case. Closer examination of Fig. 6 shows that the spray combustion region is radially wider but penetrates to a shorter distance axially in the LES case. This implies that the mixing process is slower in the LES case at this early

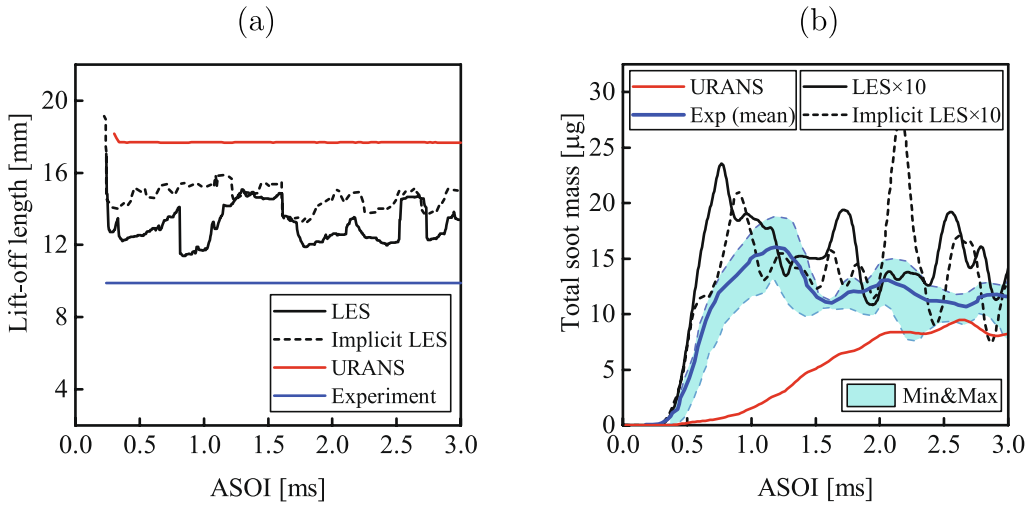

Fig. 5. Comparison of (a) the temporal evolution of lift-off length between LES, implicit LES, URANS, and experimental mean values and (b) soot mass evolution between LES, implicit LES, URANS, and experimental mean values.

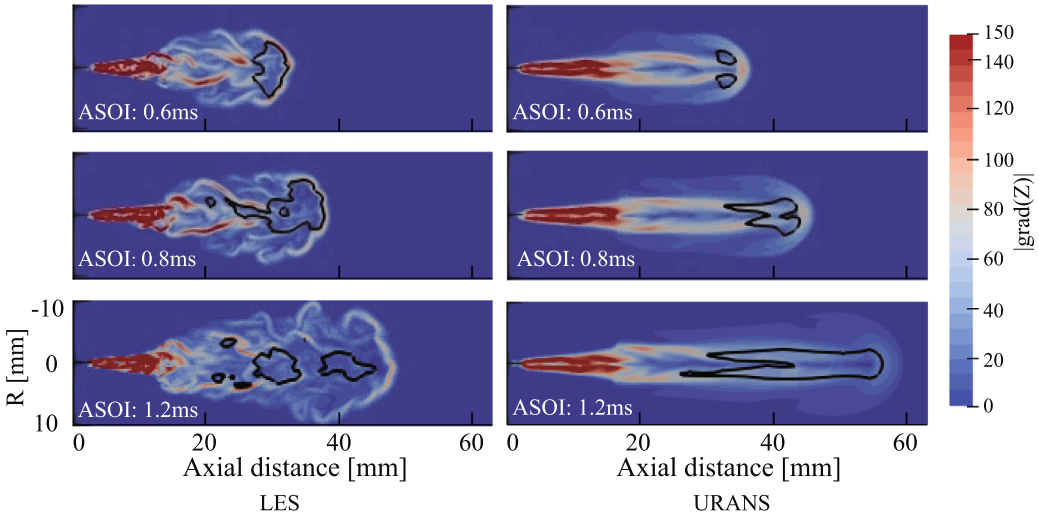

Fig. 6. Comparison of gradient of mixture fraction (Z) between the LES and URANS cases. Black line is the iso-line of soot volume fraction of 10^{-6}, which envelops the high soot volume fraction region.

combustion stage. It is expected that the slower mixing process in the LES case will result in a larger favorable region for soot formation in the LES case than that in the URANS case. This leads to a more rapid soot formation in the LES case as shown in Fig. 5(b) before 0.8 ms ASOI. In order to elucidate this, the distribution of the spray region are represented as discrete probability density function (PDF) of equivalence ratio (ϕ). Distributions of discrete PDF of local ϕ for the spray region at different time instances (0.6 ms, 0.8 ms, and 1.2 ms) are shown in Fig. 7. Only the CFD cells in a region of ϕ ranging from 0.8 to 2.5 with temperature of at least 1600 K are considered in the discrete PDF calculation since no soot is observed below this temperature in this study. As depicted in Fig. 7, the discrete PDF of ϕ is higher in the LES case than that in the URANS case before 0.8 ms ASOI, which indicates that there are more favorable regions for soot formation in the LES case. This can be clearly seen in Fig. 5(b) where the soot mass increases rapidly in the LES case but much slowly in the URANS case at the early time. At 1.2 ms, the values of the discrete PDF in the URANS case are greater than those in the LES case when the ϕ is larger than 1.8. This is evidently seen in Fig. 6 where the region of SVF in the URANS case is slightly larger than that in the LES case.

Fig. 8 shows the temporal evolution of the discrete PDF of ϕ for the LES and URANS simulations. In Fig. 8(a), the discrete PDF of ϕ for different time instances are almost identical when the ϕ is larger than 1.9. It is important to note that discrete PDF of ϕ at the favorable ϕ range (i.e., ϕ larger than 1.5) for soot formation increases from 0.6 ms to 0.8 ms, and then decreases. This is hence likely the reason for the observed soot spike at around 0.8 ms in Fig. 5(b). In Fig. 8(b), the discrete PDF of ϕ at the favorable ϕ region for soot formation in the URANS simulation continues to increase until to 2.2 ms. This agrees with the associated temporal soot evolution results shown in Fig. 5(b) which shows a steady increase in the soot mass instead of a soot spike.

The net soot mass production is a result of competition between the soot formation and oxidation rates (cf. Eq. (3)). As these rates are dependent on the mass fraction of soot precursors (C_2H_2 is selected as

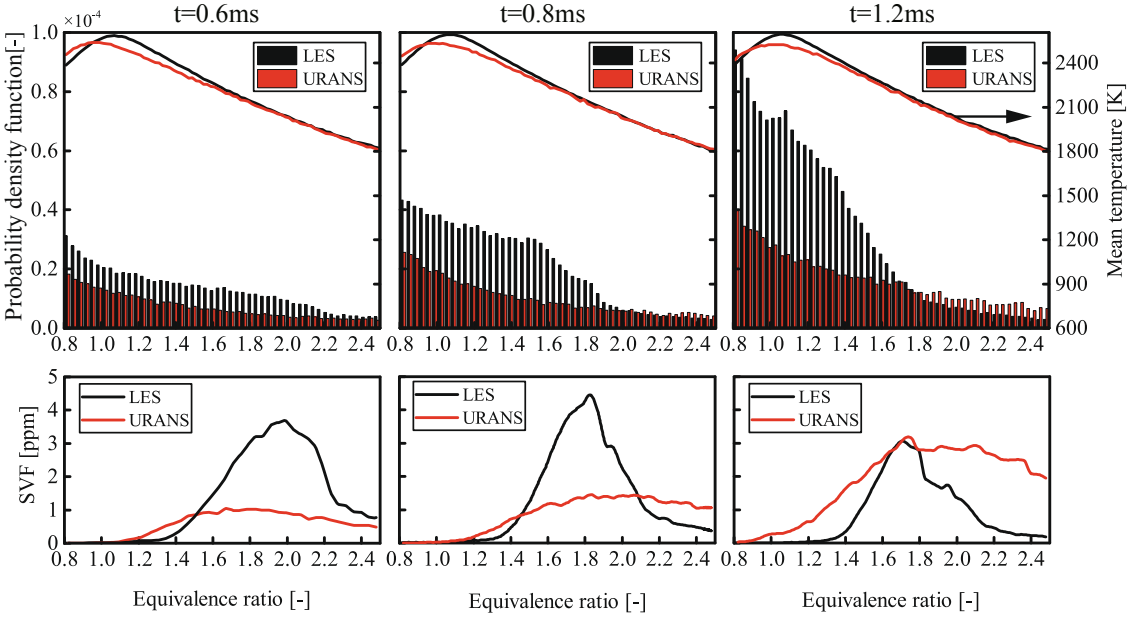

Fig. 7. Discrete probability density function of equivalence ratio (ϕ) at three different time instances. The solid lines represent the mean diffusion flame temperature conditional on ϕ. The bottom plots represent the mean soot volume fraction conditional on ϕ.

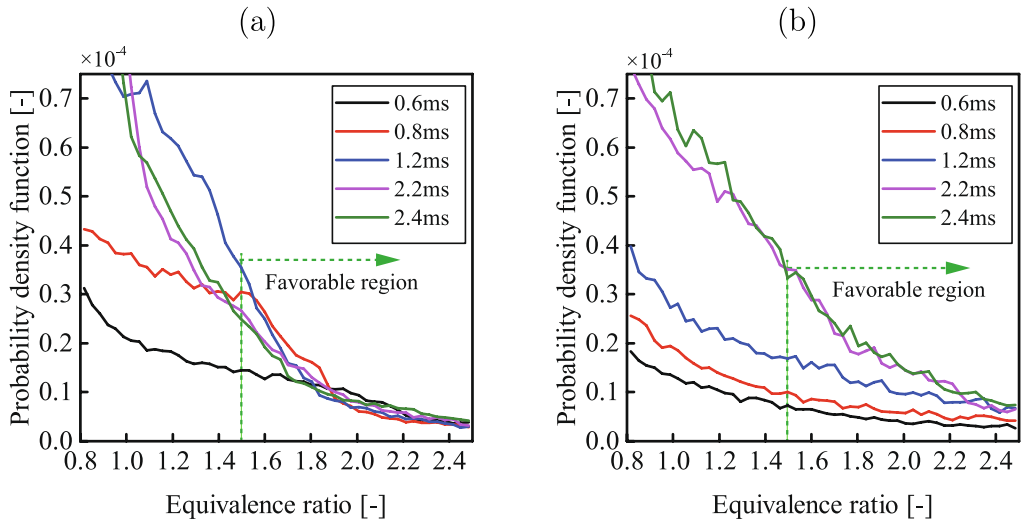

Fig. 8. Temporal evolution of discrete PDF of equivalence ratio (ϕ) for (a) LES and (b) URANS cases.

the soot precursor in the present study) and oxidizer species, the mass of C_2H_2 and OH in the domain are analyzed next. Fig. 9 shows the temporal evolution of total mass of C_2H_2 and OH for both the LES and URANS cases. As shown in Fig. 9(a), the total mass of C_2H_2 in the LES case increases rapidly and then reaches QSS; whereas it increases slowly but continuously in the URANS case and reaches QSS later than the LES case. This generally corresponds to the temporal evolution of favorable region for soot formation in both LES and URANS cases as depicted earlier in Fig. 8. Furthermore, the temporal evolution of the total mass of C_2H_2 could explain the difference of the total soot mass between the LES and URANS cases, where the total soot mass increases rapidly to reach QSS in the LES case but slowly reaches to QSS in the URANS case. Fig. 9(b) shows that the total mass of OH increases with time. It is observed that the total mass of OH in the LES case is higher than that in the URANS case. This could be explained by the fact that the high temperature, reacting zone in the LES case is thicker than that in the URANS case due to the presence of large-scale wrinkled flame surfaces as shown in Fig. 6.

The temporal evolution of the net soot production rates for the LES and URANS simulations are illustrated in Fig. 10. The rate is given as the volume-averaged rate which are also highly dependent on soot-related species concentration and surface area of soot. As the total mass of C_2H_2 stabilizes, the formation rate can no longer increase and, thus, stabilizes at around 0.75 ms. The time when C_2H_2 mass and the formation rate reach QSS corresponds to one another. However, oxidation rates are still increasing due to the increasing OH mass. This implies that the oxidation process becomes more dominant than the

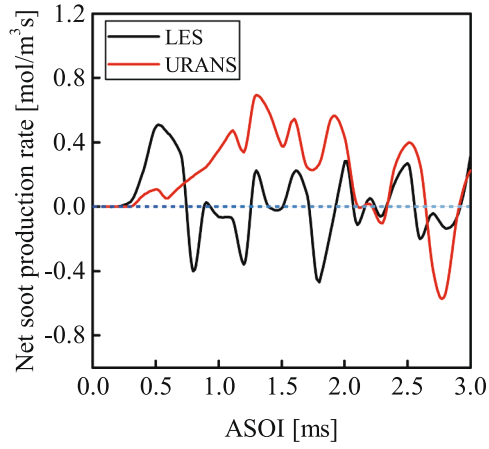

Fig. 10. Volume-averaged reaction rate of net soot production rate for LES and URANS.

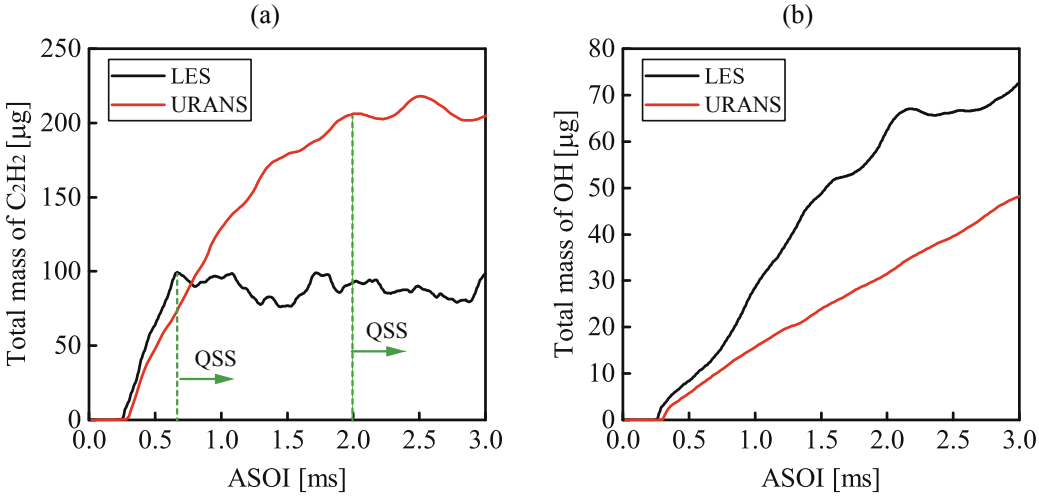

Fig. 9. Temporal evolution of (a) total mass of C_2H_2 and (b) total mass of OH for LES and URANS cases.

formation process after the stabilization of the C_2H_2 mass. As shown in Fig. 10, one can see that the net soot mass production rate in the LES case becomes negative after the total mass of C_2H_2 reaches QSS. This can be explained by the fact that LES produces more OH. It is also known that the LES model is better than URANS in capturing more detailed flow structures (e.g., large-scale vortex structures in the shear layer of the fuel jets) which lead to a more accurate prediction in local mixing [45,46]. With a better prediction in the flow structures, the LES model is able to more accurately capture the air entrainment and the local mixing between the air and soot. These collectively lead to a higher oxidation rate in the LES case. The negative value of the net soot production rate implies that the oxidation rate overtakes the formation rate, which consequently results in a decrease in the soot mass. Hence, a spike is observed in the LES case. However, the oxidation rate cannot increase further because the effective contacting area between soot and oxidizer decreases after the oxidation process becomes more dominant than the formation process, thus yielding a decrease in oxidation rate in return. Eventually, the formation and oxidation rates reach a dynamic balance, which leads to the total soot mass achieving QSS. On the other hand, the net soot mass production rate does not go negative obviously after the total mass of C_2H_2 reaches QSS in the URANS simulation. The soot mass does not form a spike due to the low formation rate at the early time. In addition, the oxidation rate does not overtake the formation rate due to the low OH mass after the formation rate reaches QSS. Hence, the formation rate and oxidation rate gradually reach a balance after the formation rate reaches QSS as shown in Fig. 10.

5. Conclusions

In this study, the early evolution of soot in the spray flame of Spray A configuration from the Engine Combustion Network (ECN) is simulated using both the large eddy simulation (LES) and Unsteady Reynolds Averaged Navier-Stokes (URANS) models in conjunction with a two-equation phenomenological soot model.

The evolution of the soot mass during the early time has two key characteristics: first, the soot mass increases rapidly; second, the soot mass reaches a peak and then decreases forming a soot spike. By coupling with the well stirred reactor (WSR), the LES approach is able to capture the transient behavior of soot mass evolution observed in the experiment. However, the transient behavior is not captured by the URANS method. The turbulence closure method is likely the reason for the unsuccessful prediction in soot transient behavior. The reason for the rapidly increasing of soot mass in the LES case is due to that the favorable region of equivalence ratio ($\phi > 1.5$) and temperature ($T > 1800$ K) for soot formation in the LES case is larger than that in the URANS case during the early time. This favorable region observed in the LES case increases and then decreases to reach a quasi-steady state (QSS). Conversely, the favorable region observed in the URANS case continues to increase. The total mass of soot precursor in the LES case reaches the QSS much earlier than that in the URANS case. Hence, a rapid increase in the soot mass is observed in the LES case. The formation rate does not increase continuously after the soot precursor reaches a plateau, whereas the oxidation rate due to OH radicals continues to increase significantly in the LES case. This leads to the oxidation process being more dominant than the formation process, which results in a decrease in the total soot mass. Hence, a soot spike is formed in the LES case. A dynamic balance between the soot formation and oxidation processes is attained as the oxidation rate is unable to increase continuously due to the decrease in the soot mass. The absence of soot spike in the URANS case is mainly due to the low OH mass produced relative to the production of C_2H_2. This results in a gradual balance between the soot formation and oxidation processes rather than a sudden shift in the dominant soot process as observed in the LES case.

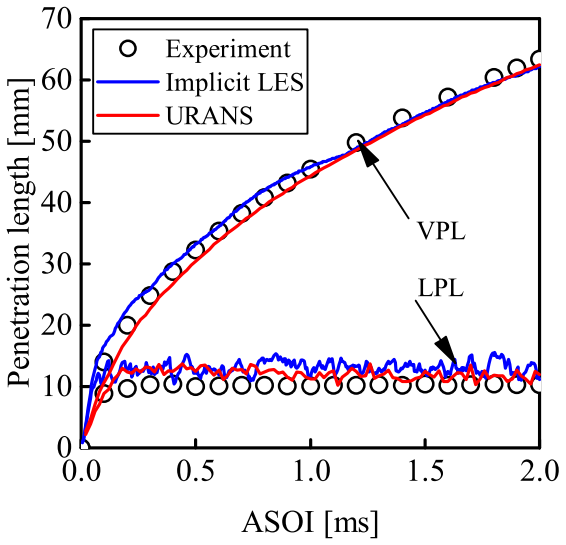

Fig. 11. Liquid and vapour penetration for URANS.

CRediT authorship contribution statement

Min Zhang: Conceptualization, Methodology, Validation, Writing - original draft. **Jiun Cai Ong:** Methodology, Supervision, Writing - review & editing. **Kar Mun Pang:** Conceptualization, Supervision, Writing - review & editing. **Xue-Song Bai:** Supervision, Writing - review & editing. **Jens Honore Walther:** Supervision, Writing - review & editing.

Declaration of Competing Interest

The authors declare that they have no known competing financial interests or personal relationships that could have appeared to influence the work reported in this paper.

Acknowledgement

Min Zhang was sponsored by China Scholarship Council (CSC). Jiun Cai Ong gratefully acknowledged the financial support from the Independent Research Fund Denmark (DFF) and MAN Energy Solutions under the Grant No. 8022-00143B. The computation was performed using Niflheim cluster at Technical University of Denmark (DTU). The authors acknowledged PRACE for awarding us access to Joliot-Curie at GENCI@CEA, France.

Appendix A. Validation of spray characteristics for URANS

As described in Section 4.4, a URANS case and an implicit LES case are compared to the LES case to investigate the underlying mechanism of soot spike. Validations of non-reacting and reacting spray characteristics for URANS cases with mesh A are presented here. The non-reacting cases here use the identical ambient conditions as that of the LES case described in Section 4.1. Note that the stripping breakup constant in the Reitz-Diwakar model [24] and the constant C_2 in the realizable $k-\varepsilon$ model [47] are calibrated to 8 and 1.8, respectively. For the implicit LES case, the computational setup is the same as in the LES case except that the sub-grid LES model is turned off. As depicted in Fig. 11, both VPL and LPL show a good agreement with the experimental data [5]. The reacting cases here employ the same ambient conditions as the LES case at 21% O_2. The IDT and LOL predicted by the

URANS are 0.30 ms and 17.6 mm, while the corresponding experiment results are 0.28 ms and 9.9 mm. Although the present simulated LOL is greater than experiment, it is almost identical to the predicted LOL in [15]. For the reacting case of implicit LES case, the simulated IDT and LOL are 0.23 ms and 14.4 mm, respectively.

References

[1] Pickett LM, Genzale CL, Bruneaux G, Malbec L-M, Christiansen C, Schramm J. Comparison of diesel spray combustion in different high-temperature, high-pressure facilities. SAE Int J Engines 2009;3(2):156–81.

[2] Kook S, Pickett LM. Soot volume fraction and morphology of conventional and surrogate jet fuel sprays at 1000-K and 6.7-MPa ambient conditions. Combust Flame 2011;33(2):2911–8.

[3] Skeen SA, Manin J, Pickett LM, Cenker E, Bruneaux G, Kondo K, Aizawa T, Westlye F, Dalen K, Ivarsson A, et al. A progress review on soot experiments and modeling in the engine combustion network (ECN). SAE Int J Engines 2016;9(2):883–98.

[4] Cenker E, Bruneaux G, Pickett L, Schulz C. Study of soot formation and oxidation in the engine combustion network (ECN), spray A: Effects of ambient temperature and oxygen concentration. SAE Int J Engines 2013;5(1):352–62.

[5] Engine combustion network, available from: https://ecn.sandia. gov/ecn-data-search/.

[6] Williams TC, Shaddix CR, Jensen KA, Suo-Anttila JM. Measurement of the dimensionless extinction coefficient of soot within laminar diffusion flames. Int J Heat Mass Transfer 2007;50:1616–30.

[7] Razak MF, Salehi F, Chishty MA. An analysis of turbulent mixing effects on the soot formation in high pressure n-dodecane sprays. Flow Turbul Combust 2019;103(3):605–24.

[8] Aubagnac-Karkar D, Michel J-B, Colin O, Darabiha N. Combustion and soot modelling of a high-pressure and high-temperature dodecane spray. Int J Engine Res 2018;19(4):434–48.

[9] Wang H, Ra Y, Jia M, Reitz RD. Development of a reduced n-dodecane-PAH mechanism and its application for n-dodecane soot predictions. Fuel 2014;136:26–36.

[10] Salehi F, Cleary MJ, Masri AR, Ge Y, Klimenko AY. Sparse-lagrangian MMC simulations of an n-dodecane jet at engine-relevant conditions. Proc Comb Inst 2017;36(3):3577–85.

[11] Wehrfritz A, Kaario O, Vuorinen V, Somers B. Large eddy simulation of n-dodecane spray flames using flamelet generated manifolds. Combust Flame 2016;167:113–31.

[12] Pei Y, Hawkes ER, Kook S. A comprehensive study of effects of mixing and chemical kinetic models on predictions of n-heptane jet ignitions with the PDF method, Flow. Turbul Combust 2013;91(2):249–80.

[13] Pei Y, Som S, Pomraning E, Senecal PK, Skeen SA, Manin J, Pickett LM. Large eddy simulation of a reacting spray flame with multiple realizations under compression ignition engine conditions. Combust Flame 2015;162:4442–55.

[14] Fernandez SF, Paul C, Sircar A, Imren A, Haworth DC, Roy S, Modest MF. Soot and spectral radiation modeling for high-pressure turbulent spray flames. Combust Flame 2018;190:402–15.

[15] Chishty MA, Bolla M, Hawkes ER, Pei Y, Kook S. Soot formation modelling for n-dodecane sprays using the transported PDF model. Combust Flame 2018;192:101–19.

[16] Lucchini T, D'Errico G, Onorati A, Frassoldati A, Stagni A, Hardy G. Modeling non-premixed combustion using tabulated kinetics and different fame structure assumptions. SAE Int J Engines 2017;10(2):593–607.

[17] Pei Y, Hawkes ER, Bolla M, Kook S, Goldin GM, Yang Y, Pope SB, Som S. An analysis of the structure of an n-dodecane spray flame using TPDF modelling. Combust Flame 2016;168:420–35.

[18] Gong C, Jangi M, Bai XS. Large eddy simulation of n-dodecane spray combustion in a high pressure combustion vessel. Appl Energy 2014;136:373–81.

[19] Pickett LM, Manin J, Genzale CL, Siebers DL, Muscculus MPB, Idicheria C. Relationship between diesel fuel spray vapor penetration/dispersion and local fuel mixture fraction. SAE Trans 2011;01-0686.

[20] Skeen SA, Manin J, Pickett LM. Simultaneous formaldehyde PLIF and high-speed schlieren imaging for ignition visualization in high-pressure spray flames. Proc Comb Inst 2015;35:3167–74.

[21] Ranz WE, Marshall Jr WR. Evaporation from drops. part 1. Chem Eng Prog 1952;48(3):141–6.

[22] D'Errico G, Lucchini T, Contino F, Jangi M, Bai X-S. Comparison of well-mixed and multiple representative interactive flamelet approaches for diesel spray combustion modelling. Combust Theor Model 2014;18(1):65–88.

[23] Desantes JM, García-Oliver JM, Novella R, Pérez-Sánchez EJ. Application of a flamelet-based CFD combustion model to the LES simulation of a diesel-like reacting spray. Comput Fluids 2020;200.

[24] Reitz RD, Diwakar R. Effect of drop breakup on fuel sprays. SAE Tech Paper Ser 1986;860469:1–10.

[25] Paul C, Fernandez SF, Haworth DC, Roy S, Modest MF. A detailed modeling study of radiative heat transfer in a heavy-duty diesel engine. Combust Flame 2019;200:325–41.

[26] Mukut KM, Roy SP. Effect of o2 concentration in ambient mixture and multiphase radiation on pollutant formation in ECN spray A. Combust Theor Model 2020;24:549–72.

[27] Jangi M, D'Errico G, Bai X-S, Lucchini T. Numerical simulation of the ECN spray A using multidimensional chemistry coordinate mapping: n-dodecane diesel combustion. SAE Tech Pap 2012;01-1660.

[28] Liu K, Haworth DC, Yang X, Gopalakrishnan V. Large-eddy simulation of motored flow in a two-valve piston engine: POD analysis and cycle-to-cycle variations. Flow Turbul Combust 2013;91(2):1–31.

[29] Senecal PK, Pomraning E, Richards KJ, Som S. An investigation of grid convergence for spray simulations using an LES turbulence model. SAE Techn Pap 2013;01-1083.

[30] Liu AB, Mather D, Reitz RD. Modeling the effects of drop drag and breakup on fuel sprays. SAE Trans. 1993:83–95.

[31] Bharadwaj N, Rutland CJ. A large-eddy simulation study of sub-grid two-phase interaction in particle-laden flows and diesel engine sprays. Atomiz Sprays 2010;20.

[32] Pang KM, Jangi M, Bai X-S, Schramm J. Evaluation and optimization of phenomenological multi-step soot model for spray combustion under diesel engine-like operating conditions. Combust Theor Model 2015;19(3):279–308.

[33] Yao T, Pei Y, Zhong B-J, Som S, Lu T, Luo KH. A compact skeletal mechanism for n-dodecane with optimized semi-global low-temperature chemistry for diesel engine simulations. Fuel 2017;191:339–49.

[34] Wang H, Reitz RD, Yao M, Yang B, Jiao Q, Qiu L. Development of an n-heptane-n-butanol-PAH mechanism and its application for combustion and soot prediction. Combust Flame 2013;160(3):504–19.

[35] Pang KM, Jangi M, Bai X-S, Schramm J. Investigation of chemical kinetics on soot formation event of n-heptane spray combustion. SAE Techn Pap 2014;01-1054.

[36] Jangi M, Yu R, Bai X-S. Development of chemistry coordinate mapping approach for turbulent partially premixed combustion. Flow Turbul Combust 2013;90(2):285–99.

[37] Jangi M, Bai X-S. Multidimensional chemistry coordinate mapping approach for combustion modelling with finiterate chemistry. Combust Theor Model 2012;16:1032–109.

[38] Jangi M, Altarawneh M, Glugogorski BZ. Large-eddy simulation of methanol pool fires using an accelerated stochastic fields method. Combust Flame 2016;173:89–98.

[39] Hadadpour A, Jangi M, Pang KM, Bai XS. The role of a split injection strategy in the mixture formation and combustion of diesel spray: A large-eddy simulation. Proc Combust Inst 2019;37(4):4709–16.

[40] Leung KM, Lindstedt RP, Jones W. A simplified reaction mechanism for soot formation in nonpremixed flames. Combust Flame 1991;87:289–305.

[41] Pope SB. Ten questions concerning the large-eddy simulation of turbulent flows. New J Phys 2004;6:1–24.

[42] Varna A, Wehrfritz A, Hawkes ER, Cleary MJ, Lucchini T, D'Errico G, Kook S, Chan QN. Using ducted fuel injection to attenuate or prevent soot formation in mixing-controlled combustion strategies for engine applications. Proc Combust Inst 2019;37:3263–70.

[43] Gehmlich R, Mueller C, Ruth D, Nilsen C, Skeen S, Manin J. Using ducted fuel injection to attenuate or prevent soot formation in mixing-controlled combustion strategies for engine applications. Appl Energy 2018;226:1169–86.

[44] Pang KM, Poon HM, Ng HK, Gan S, Schramm J. Soot formation modeling of n-dodecane and diesel sprays under engine-like conditions. SAE Trans 2015.

[45] Jhavar R, Rutland CJ. Using large eddy simulations to study mixing effects in early injection diesel engine combustion. SAE Trans 2006.

[46] Jhavar R. Using large eddy simulations to study diesel di-hcci engine flow structure, mixing and combustion. University of Wisconsin-Madison; 2007.

[47] Shih T-H, Liou WW, Shabbir A, Yang Z, Zhu J. A new $k-\epsilon$ eddy viscosity model for high Reynolds number turbulent flows. Comput Fluids 1995;24(3):227–38.